Underwater 3D Scanner Model Using a Biaxial MEMS Mirror

MIGUEL CASTILLÓN[ID]1, **ALBERT PALOMER**[ID]2, **JOSEP FOREST**[ID]1,
AND PERE RIDAO[ID]1, **(Member, IEEE)**
1Computer Vision and Robotics Research Institute (VICOROB), University of Girona, 17003 Girona, Spain
2IQUA Robotics SL, 17003 Girona, Spain

Corresponding author: Miguel Castillón (miguel.castillon@udg.edu)

ABSTRACT Underwater 3D laser scanners are an essential type of sensor used by unmanned underwater vehicles (UUVs) for operations such as navigation, inspection and object recognition and manipulation. These sensors need to be able to provide highly accurate 3D data at fast refresh rates in order to accomplish these tasks. Usually, these scanners rely on a rotating mirror actuated by a galvanometer. However, the light planes steered by this type of mirrors are typically deformed into cones due to refraction. In order to produce accurate results, this distortion needs to be taken into account, which increases the computational cost of the 3D reconstruction. A novel approach consisting in using a biaxial MEMS mirror is proposed in this paper. The second rotational degree of freedom of the mirror can be used to project optimally curved light shapes, so that the refraction process transforms them into planes. Being able to model the light surfaces as planes rather than cones can significantly reduce the computation time of the 3D reconstruction. In order to do so, an exhaustive model of the complete light trajectories is presented. To the best of the authors' knowledge, this paper constitutes the first attempt to model and counteract the distortion in the scanning pattern introduced by a biaxial mirror and a double refraction process in the context of underwater robotics.

INDEX TERMS Mobile robotics, autonomous robots, underwater robotics, 3D laser scanner, 3D sensing.

I. INTRODUCTION

Unmanned underwater vehicles (UUVs) are being increasingly used in industry out of safety and cost reasons. Particularly, autonomous underwater vehicles (AUVs) are already performing tasks such as object recognition [1], inspection [2], manipulation [3] or navigation [4]. Sensing their surroundings is essential for them to achieve their tasks. Therefore, they are usually equipped with some type of 3D sensor, which are mainly based either on acoustic (SONAR) or light signals (LiDAR). The main advantage of optical sensors is that they can provide a much higher lateral resolution and refresh rate [5]. Their relatively short range is usually enough for intervention tasks, since the robot needs to get close to the target.

Underwater 3D sensing using optical sensors has two main challenges: the fast attenuation rate of light in water and the distortion introduced by refractive elements.

The associate editor coordinating the review of this manuscript and approving it for publication was Jing Yan[ID].

Therefore, 3D sensing technology developed for in-air applications cannot be directly submerged and used for underwater tasks. Some authors have tried to adapt commercial in-air scanners to the underwater domain [6]–[8]. Even though their low price could make them useful for certain applications, their low range and accuracy would not suffice for real operations such as mapping or object manipulation. Consequently, custom-made sensors need to be developed for underwater tasks. Moreover, they should achieve high performance regarding two main aspects: high accuracy and fast refresh rate.

Underwater 3D scanners designed for inspection and manipulation typically use a rotating mirror actuated by a galvanometer [9], [10]. However, the flat refractive surfaces that seal the scanner deform the outcoming light planes into cones [11]. Modelling these cones in order to produce accurate results is possible but entails a higher computational cost. This problem can be tackled by approaching the refraction process the other way around: if the projected planes result in cones when entering the water, is there any surface that

gets transformed into a plane due to the refraction process? In order to find those surfaces, a novel approach consisting in using a biaxial microelectromechanical system (MEMS) mirror is proposed in this paper. MEMS mirrors are small-sized mirrors whose actuator transforms the applied voltage into rotation angle. Due to their small inertia, they can rotate faster than typical mirrors. They are further reviewed in section II-B. The second rotational degree of freedom of the mirror can be used to project optimally curved light shapes, so that they are refracted into planes. In order to do so, an exhaustive model of the complete light trajectories and its results using synthetic data are presented in the following sections.

Modelling the light surface as a plane rather than as an elliptic cone constitutes an advantage from the point of view of the computational cost. Triangulation-based 3D laser scanners reconstruct the shape of the 3D target by triangulating each illuminated pixel on the camera image with the corresponding laser surface. This means that the position of each 3D point in the point cloud is computed by intersecting a line and the modelled surface. Taking into account that a typical value of point cloud density in this type of scanners is 500k points per scan, reducing the computational complexity of the reconstruction of each point is of great importance. When using an elliptic cone, this triangulation consists in solving a quadratic equation and choosing the appropriate value from the two-valued solution [11]. On the other hand, triangulation using a plane boils down to simply solving a linear equation. This reduces the computational time of the 3D reconstruction of every point by a factor of 8 in our current implementation.

The main contribution of this paper is presenting a model to compensate for the distortion introduced by the flat refractive surface, so that the light surface entering in the water can be modelled as a plane rather than as an elliptic cone. This way, the computational time used for the 3D reconstruction of the scene can be significantly reduced without losing accuracy. This claim is further developed by means of exhaustive simulations, which also aim at modelling the non-ideal behaviour of the scanner. To the best of the authors' knowledge, this paper constitutes the first attempt to model and counteract the distortion in the scanning pattern introduced by a biaxial mirror and a double refraction process in the context of underwater robotics.

The paper is structured as follows. First, a literature review on different topics related to this research is summarized in section II. Then, the proposed model is presented in section III. The non-ideal behaviour of the mirror is simulated in section IV in order to quantify the magnitude of the errors related to it. Finally, the conclusions drawn are listed in section V. As support notes, basic geometrical concepts are refreshed in appendix A.

II. RELATED WORK

This section studies the state of the art regarding 3D laser scanners. First, literature regarding underwater scanners is summarized in section II-A, including descriptions and

examples of different types of sensors. Then, in-air solutions that may be proved useful if adapted to the underwater domain are studied in section II-B.

A. UNDERWATER 3D LASER SCANNERS

Optical 3D sensors are usually divided into active and passive. An underwater sensor is active if it projects light patterns onto the scene in a controlled way [12]. These patterns can be spatial (a point, a line or more complex shapes) and/or temporal. In active techniques, the information given by the structure of the pattern is key to reconstruct the scene in 3D. Laser scanners, which is the topic of this section, are therefore active sensors. A complete survey on underwater active optical sensors can be found in a previous work [13]. On the other hand, a passive sensor reconstructs its surrounding scene in 3D using information other than the structure of the light. This information comes from different simultaneous viewpoints or from the movement between consecutive image frames. Well-known passive techniques in underwater environments are stereo vision [12], [14] and structure from motion (SfM) [15], [16].

Active optical 3D sensors can be further classified depending on how they project light onto the scene. One of the main approaches can be categorized under the "one-shot" label [17]–[20]. These sensors illuminate the whole scene at once with a certain pattern. The acquisition time for the whole scene is therefore extremely short. For this reason, they are suitable to scan scenes in which high dynamics are present. However, they can only provide limited lateral resolution (perpendicularly to the depth direction).

Another popular type of sensors are laser line scanners (LLSs). These scanners generally use laser line modules, which project a light plane onto the target. One of their main advantages when compared to one-shot scanners is their high point cloud density. However, since they need a certain amount of time to sweep the laser along the scene of interest, their 3D reconstructions may be distorted when high dynamics are present. For this reason, fast scanning frequencies are usually preferred.

Some LLSs [21]–[24] do not steer the laser plane, so that its relative pose with respect to the camera is constant. This way, they achieve a robust performance, since the number of parameters to be calibrated is relatively low. Moreover, by making the laser plane enter the viewport perpendicularly, the effects of the double refraction are minimized. However, the speed at which they can scan a certain area is totally dependent on the speed of the platform used to steer the scanner. They are typically mounted on static rotational heads [25] or attached to the bottom of a vessel or an UUV facing downwards, projecting the laser plane in the direction perpendicular to the movement of the platform.

In order to increase the size of the area that can be scanned per second, some authors include some kind of laser steering mechanism in their LLSs. One of the most well-known approaches is reflecting the laser plane on a rotating mirror actuated by a galvanometer [9], [10]. The mirror is normally

placed inside the sealed case, so the friction caused by the surrounding air is negligible compared to water. This small friction along with the small inertia of the mirror allows it to achieve relatively high rotation speeds, which increases notably the area that be scanned per second.

However, this approach presents some issues. First, deflecting the laser ray direction makes it enter the viewport at a non-perpendicular angle (assuming a flat viewport is used). Therefore, the double refraction process causes the laser ray travelling in water to have another different direction. Moreover, the refractive viewport deforms the original laser plane into a cone, as described in [11]. These two non-ideal behaviours need to be taken into account in order to produce accurate 3D reconstructions. Doing so, nonetheless, is computationally expensive. Using a dome viewport can in principle be a solution to these problems, since the laser ray would theoretically always intersect the viewport plane perpendicularly. In reality, however, aligning the center of curvature of the viewport with the center of rotation of the mirror is not straightforward, so distortions may not disappear completely. Second, introducing a new element makes the sensor model grow with more parameters, so its calibration becomes more difficult.

Another approach to designing an underwater scanner different from a LLS was followed in [26]. Instead of using a laser line module with a 1-DoF mirror, they used a laser pointer reflected on a 2-DoF polygon mirror.

B. BIAXIAL-MIRROR SCANNERS FOR IN-AIR APPLICATIONS

One of the main drives for the research of 3D scanners outside water is the automotive industry. The development of sensors aimed at improving autonomous capabilities of cars is a rapidly growing field. More particularly, LiDAR-based navigation is one of the current main applications of these sensors [27]–[32]. Most of the commercial LiDARs use some kind of rotating mirror. Currently, an increasingly popular element to produce a small-sized LiDAR are MEMS mirrors [33].

MEMS mirrors are small-sized mirrors whose actuator transforms the applied voltage into rotation angle. Due to their small inertia, they can rotate faster than typical mirrors. Moreover, they are usually biaxial: they can rotate around two perpendicular axes. They can work in two different regimes: linear and resonant. The resonant regime occurs around the first resonance frequency of one of the axes of the mirror (typically a few kHz) [34], [35]. In this operation mode, one of the axes vibrates fast at its resonance frequency sweeping the target while the other axis controls the inclination of the projected line. This mode is known as raster scanning, which means that the scene is scanned from beginning to end. On the other hand, linear operation on both axes can only provide a slower scanning speed. However, it has the advantage of being able to continuously project the laser ray at arbitrary directions. Consequently, this regime can project arbitrary patterns at different resolutions. MEMS mirrors have been

recently studied in [36]–[38]. It is very relevant to know that the rotations of biaxial mirrors introduce distortions in the light patterns, as studied in [39].

Recently, there have also been advances on so-called solid-state LiDARs, which deflect the laser ray without using any moving part. They typically use electro-optic deflectors (EODs) or acousto-optic deflectors (AODs), which can accurately deflect the ray at very high speeds. Despite their potential advantages, EODs and AODs currently present very strong limitations, such as extremely narrow field of view (FoV) and limited wavelengths [40], [41].

III. MODEL

This section develops the proposed geometrical model of the underwater laser scanner. It is structured as follows. First, the description of the model elements and parameters is done in section III-A. Then, the implementation of the model is described in detail in section III-B. Finally, the inverse use of the model to compute the required pairs of mirror angles is explained in section III-C.
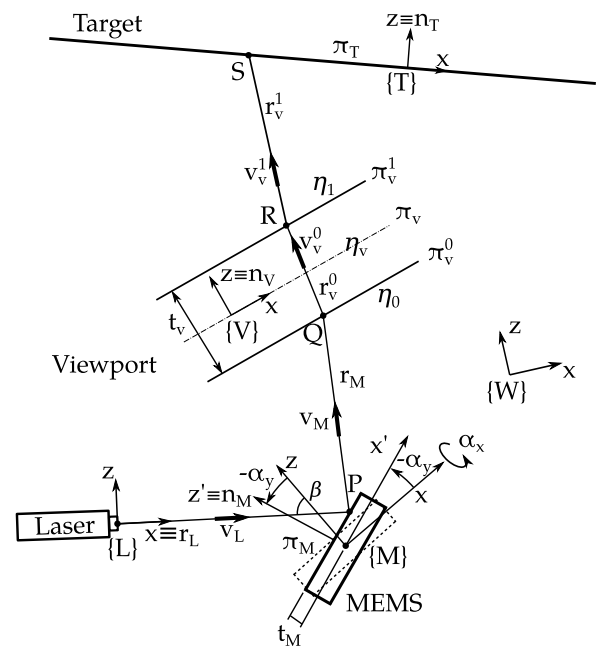
FIGURE 1. Underwater laser scanner model. It is drawn in 2D only for the sake of simplicity. In reality, the *y* directions of the different coordinate frames need not be parallel.

A. MODEL PARAMETERS

Figure 1 shows the model of the underwater laser scanner, which is composed of 4 elements: a laser point source, a biaxial mirror, a flat viewport used as transparent window separating two different media, and a target to be scanned. The following assumptions have been made when building the model:

1) LASER

The laser is considered a point light source. Its outcoming ray is modelled as a line, which represents the longitudinal

middle axis of the real ray. It is aligned with the x axis of its local reference frame $\{L\}$.

2) MEMS

The MEMS mirror is modelled as a rectangular prism that can be rotated around two of its local axes (x and y) by the angles α_x and α_y, respectively. The origin of its local reference frame $\{M\}$ is placed at the center of rotation. The reflective surface of the mirror is then represented by the plane π_M, which is at a distance t_M of the center of rotation, and whose normal is aligned with the local direction z'.

3) VIEWPORT

The flat viewport is also modelled as a rectangular prism. The middle XY plane π_V is the symmetry plane that goes through the origin of its local reference frame $\{V\}$. Parallel to it are the inner and the outer refraction planes (π_V^0 and π_V^1, respectively) at a distance $t_V/2$ from it. Both of them deflect the light ray according to the refraction indices η_0, η_V and η_1. The normal vectors of the 3 planes are parallel to the local z direction.

4) TARGET

The target object to be scanned is represented by a plane, π_T. It goes through the origin of its local reference frame $\{T\}$ and its normal is aligned with the local z direction.

TABLE 1. Model parameters.

Element	Parameters
Laser	Pose ξ_L
Mirror	Pose ξ_M Distance to center of rotation t_M Angle pair $[\alpha_x \ \alpha_y]$
Viewport	Pose ξ_V Thickness t_V Indices of refraction η_0, η_V, η_1
Target	Pose ξ_T

The different elements of the model are parameterized according to table 1. Once the model has been built, the only parameters that can be actuated in order to perform the scan of a target are $[\alpha_x \ \alpha_y]$. Therefore, all the rest are assumed constant and defined as $\Gamma = [\xi_L \ \xi_M \ t_M \ \xi_V \ t_V \ \eta_0 \ \eta_V \ \eta_1 \ \xi_T]$.

As a side note, it should be highlighted that the presented model for underwater scanning can be immediately applied to in-air scanning without viewport by setting $\eta_0 = \eta_V = \eta_1$.

B. APPLYING THE MODEL

The first goal of the model is to express the position of the scanned point S with respect to the world reference frame as a function of all the model parameters. Formally, ${}^{\{W\}}S = f\left(\Gamma, [\alpha_x \ \alpha_y]\right)$. Since all the parameters in Γ are assumed constant, for a given configuration of the scanner the final point only depends on the actuated angles of the mirror:

$$
{}^{\{W\}}S = f\left(\alpha_x, \alpha_y\right) \tag{1}
$$

Algorithm 1 Computing S in $\{W\}$ as a Function of the Model Parameters

1: **procedure** PROJECT(α_x, α_y)
2:     $O \leftarrow [0\ 0\ 0]^T$
3:     $e_x \leftarrow [1\ 0\ 0]^T$
4:     $e_z \leftarrow [0\ 0\ 1]^T$
5:
6:     // Laser
7:     ${}^{\{L\}}r_L \leftarrow (O, e_x)$
8:     $r_L \leftarrow \xi_L \oplus {}^{\{L\}}r_L$
9:
10:     // Mirror
11:     $z' \leftarrow R(\alpha_x, \alpha_y)z$
12:     ${}^{\{M\}}\pi_M \leftarrow (z', t_M)$
13:     $\pi_M \leftarrow \xi_M \oplus {}^{\{M\}}\pi_M$
14:     $n_M \leftarrow \text{NORMAL}(\pi_M)$
15:     $P \leftarrow \text{INTERSECT}(r_L, \pi_M)$ ▷ eq. (20)
16:     $v_M \leftarrow \text{REFLECT}(v_L, n_M)$ ▷ eq. (18)
17:     $r_M \leftarrow (P, v_M)$
18:
19:     // Viewport
20:     ${}^{\{V\}}\pi_V^0 \leftarrow (z, -t_V/2)$
21:     ${}^{\{V\}}\pi_V^1 \leftarrow (z, t_V/2)$
22:     $\pi_V^0 \leftarrow \xi_V \oplus {}^{\{V\}}\pi_V^0$
23:     $\pi_V^1 \leftarrow \xi_V \oplus {}^{\{V\}}\pi_V^1$
24:     $n_V \leftarrow \text{NORMAL}(\pi_V^0)$
25:     $Q \leftarrow \text{INTERSECT}(r_M, \pi_V^0)$ ▷ eq. (20)
26:     $v_V^0 \leftarrow \text{REFRACT}(v_M, n_V, \eta_0, \eta_V)$ ▷ eq. (19)
27:     $r_V^0 \leftarrow (Q, v_V^0)$
28:     $R \leftarrow \text{INTERSECT}(r_V^0, \pi_V^1)$ ▷ eq. (20)
29:     $v_V^1 \leftarrow \text{REFRACT}(v_V^0, n_V, \eta_V, \eta_1)$ ▷ eq. (19)
30:     $r_V^1 \leftarrow (R, v_V^1)$
31:
32:     // Target
33:     ${}^{\{T\}}\pi_T \leftarrow (O, e_z)$
34:     $\pi_T \leftarrow \xi_T \oplus {}^{\{T\}}\pi_T$
35:     $S \leftarrow \text{INTERSECT}(r_V^1, \pi_T)$ ▷ eq. (20)
36: **end procedure**

The implementation of function f is conceptually shown in algorithm 1. From now on, all the variables are assumed to be referred to the world coordinate frame $\{W\}$ unless otherwise explicitly stated. Lines are defined by a point and a vector and planes by a normal vector and the distance to the reference frame (see section A-3). Please, bear in mind that this implementation is conceptual. For instance, $r_L \leftarrow \xi_L \oplus {}^{\{L\}}r_L$ in line 8 is meant to signify that the laser ray r_L in the world coordinate frame is obtained from the laser pose ξ_L and its equation relative to the local frame ${}^{\{L\}}r_L$. In reality, this operation is implemented as explained in section A-4.

The rotation matrix $R(\alpha_x, \alpha_y)$ in line 11 is built as a multiplication of two matrices: one expressing the rotation around the y axis of the mirror and another around x. The mirror is considered to first rotate around the y axis an angle α_y.

Then, it rotates around the unrotated x axis an angle α_x. Since both rotations occur around the original axes, the 3×3 rotation matrix on the y axis $\boldsymbol{R}_y(\alpha_y)$ is premultiplied by the 3×3 rotation matrix on the x axis $\boldsymbol{R}_x(\alpha_x)$:

$$\boldsymbol{R}(\alpha_x, \alpha_y) = \boldsymbol{R}_x(\alpha_x)\, \boldsymbol{R}_y(\alpha_y) \tag{2}$$

C. APPLYING THE REVERSE MODEL

The proposed model can also be used to solve the inverse problem: given a point to be scanned $\boldsymbol{S}$, which angles $[\alpha_x\ \alpha_y]$ should the mirror be rotated? This is a highly relevant problem because solving it allows to project the laser ray in any arbitrary direction inside its FoV. This is directly applicable to 3D scanning: when scanning a target, the laser ray must be steered in order to project a given pattern onto the scene. This pattern is a set of known setpoints that the laser needs to illuminate in a particular order. By using a biaxial MEMS mirror and solving the aforementioned inverse problem, any arbitrary pattern can in principle be projected.

Solving the inverse problem means inverting the function f in equation (1). However, doing so analytically is a very cumbersome task because the variables $[\alpha_x\ \alpha_y]$ appear multiple times with different exponents and inside different trigonometric functions. Therefore, a numerical approach is followed.

1) ONE SINGLE POINT

The pair of angles $[\alpha_x^*\ \alpha_y^*]$ that achieve the projection of $\boldsymbol{S}$ on the target must comply with the equation

$$[\alpha_x^*\ \alpha_y^*] = f^{-1}(\boldsymbol{S}). \tag{3}$$

They can be found iteratively by using the non-linear least-squares Ceres solver [42]. In order to do so, the residual error to be minimized is

$$r = ||\boldsymbol{S} - f(\alpha_x, \alpha_y)||^2 \tag{4}$$

Like in any iterative solver, an initial guess is required. In this problem, starting with $\alpha_x = \alpha_y = 0°$ is usually good enough for the solver to converge to the solution.

2) APPROXIMATED FUNCTION

Real 3D scanning patterns can be made up of hundreds or thousands of setpoints. A straightforward way to compute the required angle pairs would be computing each pair of angles corresponding to each setpoint, as seen before. This approach, however, would not be efficient. Finding a more efficient approach could in principle allow the projection pattern to be changed online. This could enable the sensor to increase its resolution in interesting areas of the FoV as it scans or to decrease it in order to speed up the 3D reconstruction.

An arbitrary pattern Ω consisting of n points can be expressed as:

$$\Omega = f(\boldsymbol{\alpha}), \tag{5}$$

where

$$\Omega = \begin{bmatrix} \boldsymbol{S}^1 \\ \boldsymbol{S}^2 \\ \vdots \\ \boldsymbol{S}^n \end{bmatrix} \text{ and } f(\boldsymbol{\alpha}) = \begin{bmatrix} f(\alpha_x^1, \alpha_y^1) \\ f(\alpha_x^2, \alpha_y^2) \\ \vdots \\ f(\alpha_x^n, \alpha_y^n) \end{bmatrix}. \tag{6}$$

Consequently, in order to project the pattern, the set of needed angle pairs can be computed as

$$\boldsymbol{\alpha} = f^{-1}(\Omega). \tag{7}$$

Like before, finding the analytical expression of the inverse function f^{-1} is cumbersome. Instead, it would be highly beneficial to find a simpler, approximated function g that yielded approximated values for the angle pair $[\tilde{\alpha}_x\ \tilde{\alpha}_y]$ corresponding to an arbitrary projection point $\boldsymbol{S}$:

$$[\tilde{\alpha}_x\ \tilde{\alpha}_y] = g(\boldsymbol{S}) \tag{8}$$

These values would be then used to project an approximated setpoint $\tilde{\boldsymbol{S}}$, which would be close enough to the original $\boldsymbol{S}$:

$$\tilde{\boldsymbol{S}} = f(\tilde{\alpha}_x, \tilde{\alpha}_y) \approx \boldsymbol{S} \tag{9}$$

This would be done for all the points in the pattern:

$$\tilde{\Omega} = f(g(\Omega)) \approx \Omega \tag{10}$$

More specifically, the function g is chosen to be a 5th polynomial on S_x and S_y:

$$\tilde{\alpha}_x = g(S_x, S_y, \boldsymbol{\sigma}_x) \tag{11}$$
$$\tilde{\alpha}_y = g(S_x, S_y, \boldsymbol{\sigma}_y) \tag{12}$$

$\boldsymbol{\sigma}_x$ and $\boldsymbol{\sigma}_y$ are the coefficient vectors of the polynomial that yield the corresponding approximated angles $\tilde{\alpha}_x$ and $\tilde{\alpha}_y$, respectively. The z component of $\boldsymbol{S}$ is not used because it is a redundant parameter that is determined by the position of the target plane π_T.

The coefficient vectors $\boldsymbol{\sigma}_x$ and $\boldsymbol{\sigma}_y$ are found numerically using Ceres [42]. First, an arbitrary pattern Ω containing n setpoints is defined. Then, the residual passed to the solver is

$$r = \sum_{0 \leq i \leq n} ||\boldsymbol{S}^i - f(\tilde{\alpha}_x^i, \tilde{\alpha}_y^i)||^2, \tag{13}$$

where $\tilde{\alpha}_x^i$ and $\tilde{\alpha}_x^i$ are computed using equations (11) and (12). The resulting joint formal expression for the optimized coefficient vectors $\left[\boldsymbol{\sigma}_x^*\ \boldsymbol{\sigma}_y^*\right]$ is then:

$$\left[\boldsymbol{\sigma}_x^*\ \boldsymbol{\sigma}_y^*\right] = \underset{\boldsymbol{\sigma}_x, \boldsymbol{\sigma}_y}{\arg\min}$$
$$\sum_{0 \leq i \leq n} ||\boldsymbol{S}^i - f\left(g\left(S_x^i, S_y^i, \boldsymbol{\sigma}_x\right),\ g\left(S_x^i, S_y^i, \boldsymbol{\sigma}_y\right)\right)||^2 \tag{14}$$

In order to evaluate the performance of the proposed approximated function, a pattern consisting in 50×50 equidistant setpoints spread over the whole FoV is used. Please note that these are waypoints through which the scanning pattern will pass. The values of all the different sensor

parameters are gathered in table 2. Please note that the target is at a distance of 1 m from the MEMS.

Computing each angle pair corresponding to each of the setpoints takes around 7 s for such a pattern. If the pattern were required to change, new angles would need to be computed once again, unless some of the setpoints could be reused or interpolated. Using the approximated approach, the required time to compute all the angles is greatly reduced to 7 ms for the same pattern. Regarding accuracy, the maximum and average point-to-point distances between the desired and the approximated patterns are 0.013 mm and 0.002 mm, respectively. The resulting angles computed using the approximated function are also very similar to the ones obtained point by point: their maximum and average differences are 0.12° and 0.07°, respectively. These results confirm that the 5$^{\text{th}}$-order polynomial is a suitable approximation function for f^{-1}, since it allows to reduce computation time while keeping a very high accuracy. Computing the coefficient vectors σ_x and σ_y takes around 1 minute, but it only needs to be done once because they would only vary if some of the sensor parameters changed.

The order of the polynomial g has been chosen to be 5 heuristically. Additional investigation of more potentially appropriate functions could be carried out. However, given that the evaluation times for different polynomial orders are very similar, their use would probably not increase the sensor performance noticeably.

TABLE 2. Nominal values for the model parameters. The units are millimeters for lengths and degrees for angles.

$\xi_L = [0\ 0\ 0\ 0\ 0\ 0]^T$	$\xi_M = [10\ \delta\ \delta\ 0\ \theta_M\ 0]^T$
$\xi_V = [0\ 0\ l_V\ 0\ \theta_V\ 0]^T$	$\xi_T = [0\ 0\ 1000\ 0\ \theta_T\ 0]^T$
$\delta = 0$	$\theta_M = -70$
$l_V = 100$	$\theta_V = 0$
$\theta_T = 0$	
$t_M = 0$	$t_V = 20$
$\eta_0 = 1.00$	$\eta_V = 1.51$
$\eta_1 = 1.33$	$\alpha_x, \alpha_y = [-5,\ 5]$

IV. STUDY OF PARAMETER INFLUENCE

This section is devoted to examining the influence that each one of the model parameters has on global performance. In order to study the individual effect of each parameter, they will be modified one at a time while keeping the rest constant. Let us consider a synthetic model with the nominal values of all the parameters defined in table 2. The poses ξ of all the elements are referenced to the world coordinate frame $\{W\}$. The rotation angles around the local y axes of the MEMS, viewport and target are represented with θ_M, θ_V and θ_T, respectively. δ is the displacement of the mirror reference frame $\{M\}$ in world y and z directions. l_V is the position of the reference frame of the viewport in the world z direction. A schematic top-down view of this configuration is shown
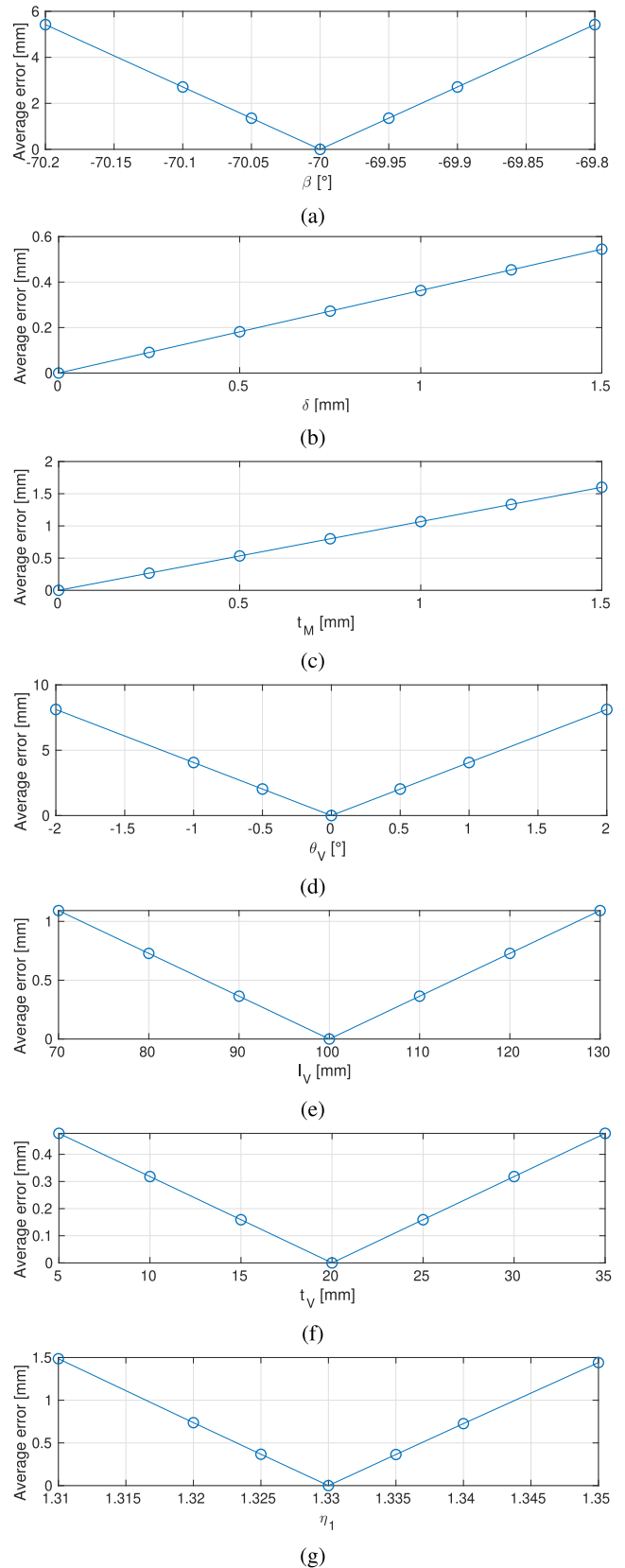
FIGURE 2. Influence of miscalibrating each parameter. Please note the different error scales in the vertical axes.
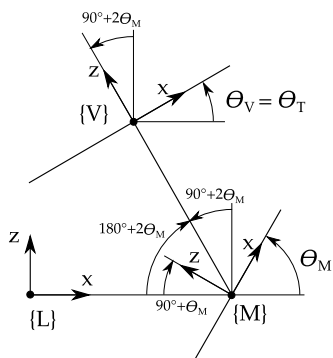
FIGURE 3. Viewport and target are kept perpendicular to the outcoming light ray for $\alpha_x = \alpha_y = 0°$ throughout the simulations. Therefore, the y angles of the viewport and target depend directly on the y angle of the MEMS. In this configuration, $\theta_V = \theta_T = 90° + 2\theta_M$. Please note that the values of angles θ_M, θ_V and θ_T as drawn in the figure would have negative sign.

in figure 3. Note that in this configuration:

$$\beta = 90° + \theta_M, \quad (15)$$

where β is the angle defined by the laser ray and the normal of the mirror plane when $\alpha_x = \alpha_y = 0$ (see figure 1).

The different indices of refraction η are chosen from air, plexiglass and water, respectively [43]. The maximum mechanical angle for both axes of the MEMS is 5°, which makes both the horizontal and vertical mechanical FoVs equal to 10°. This is a typical value for MEMS mirrors [34].

The section is structured as follows: first, the magnitude of the error that results from miscalibrating each parameter individually is reported in section IV-A. Then, other sources of error in the final projection are described in section IV-B. Finally, the effect of the parameters in the FoV of the scanner is studied in section IV-C.

A. EFFECT OF INDIVIDUAL PARAMETER MISCALIBRATION

The model presented in this paper is aimed at evaluating and reducing the projection errors of the scanner. One of the main sources of projection errors is parameter miscalibration. A parameter is miscalibrated when its actual value differs from its nominal one. The projection error introduced by this miscalibration is defined as the distance between the nominal (expected) position of a point S and its deviated (actual) position S_m.

The projection errors due to miscalibrated parameters are shown in figure 2. The metric used in all their vertical axes is the average distance between the nominal projection and the miscalibrated one for each projected point (for n waypoints in total, with $n = 100$):

$$\text{avg error} = \frac{1}{n} \sum_{0 \le i < n} \|S^i - S_m^i\| \quad (16)$$

There is a number of conclusions that can be drawn from these figures. First, it can be seen that θ_M (directly related to β, see equation (15)) is a very critical parameter: a slight

(a) $\beta = 10°$

(b) $\beta = 20°$

(c) $\beta = 45°$
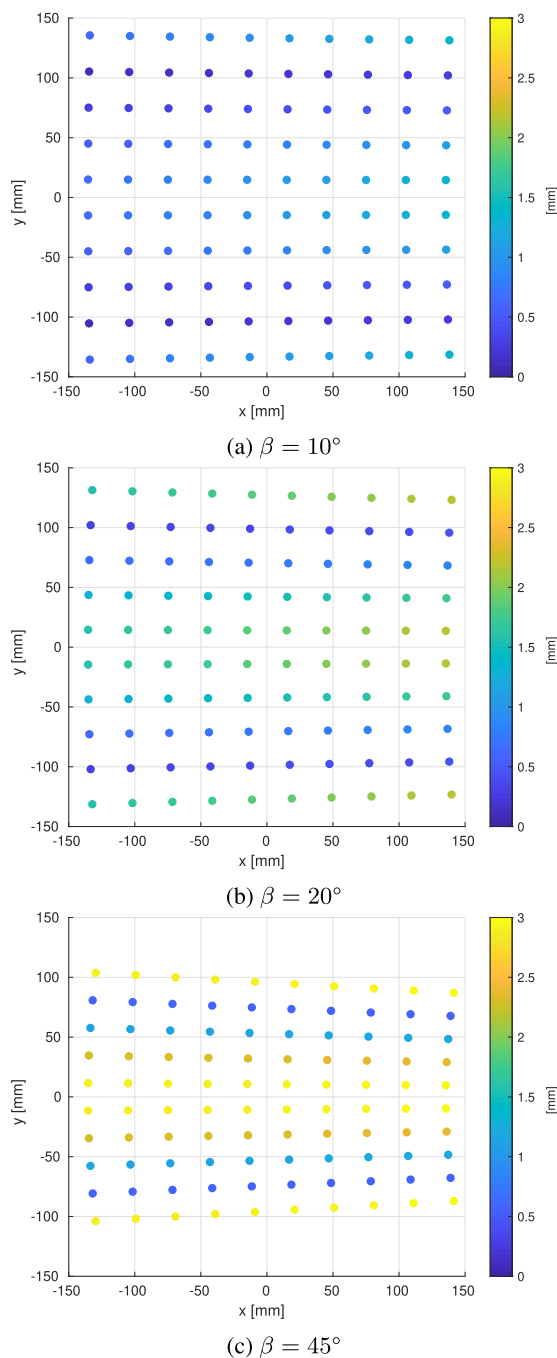
FIGURE 4. Distorted patterns for different values of β at 1 m distance. The color bar measures the distance of each point to the average x-coordinate of its corresponding vertical line.

deviation from its nominal value of only 0.2° makes the error increase rapidly (see figure 2a). Similarly, a deviation in the value of θ_V of only half a degree causes an average error well over 1 mm (see figure 2d). Regarding the index of refraction of water, it should be noted that it generally depends on different factors, such as light wavelength, salinity and temperature. For a green laser source of wavelength $\lambda = 532$ nm, the index of refraction of sea water η_1 is between 1.330 and 1.345 for a wide range of salinity values [44]. A discrepancy
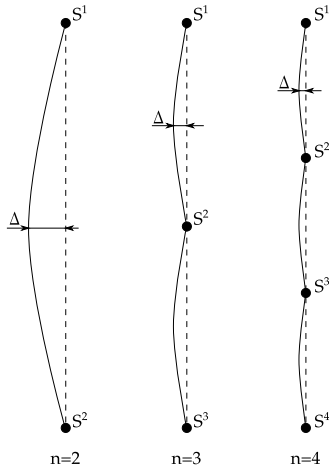
FIGURE 5. Maximum deviation Δ from the desired pattern of straight lines for an increasing number of waypoints. The curved lines show the actual light trajectories between waypoints.

of this order would entail an average error of around 1 mm (see figure 2g).

Moreover, the possible variations of δ and t_M considered are up to 1.5 mm, since that is in the order of a typical MEMS mirror diameter [34]. These values are enough to cause noticeable deviations, especially if the required precision is submillimetric (see figure 2b and 2c).

On the other hand, the influence of a slightly miscalibrated viewport thickness is not too high (1 cm of deviation entails an average error of around 0.3 mm, see figure 2f). Similarly, an error in the viewport distance of up to 1 cm would not make the average error increase further than 0.4 mm (see figure 2e). In these last two cases, standard measurement tools exist that can easily provide lengths measurements with a greater accuracy than 1 cm.

B. OTHER SOURCES OF ERROR

The presented model allows the investigation of different sources of errors other than parameter miscalibration. This section studies the magnitude of projection errors with perfectly calibrated parameters. The sources of error considered depend on the number of waypoints used per line (section IV-B1) and on the real distance to the target (section IV-B2). The aim of this section is helping to have a deeper insight on which nominal parameter values are optimal.

In the following results, both viewport and target planes are kept perpendicular to the outgoing reflected laser beam when $\alpha_x = \alpha_y = 0°$ (see figure 3). Therefore:
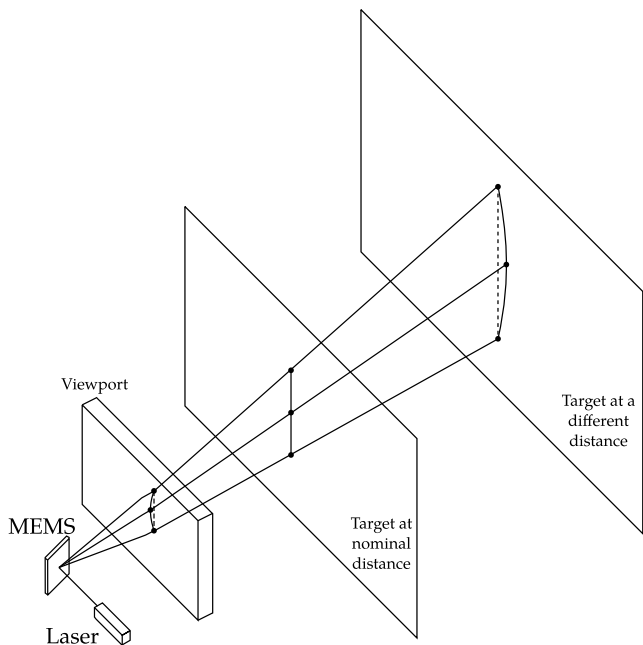
$$\theta_V = \theta_T = 90° + 2\,\theta_M \qquad (17)$$

1) NUMBER OF WAYPOINTS PER LINE

The model presented in this paper can be used to compensate for the distortions introduced by the biaxial mirror and by
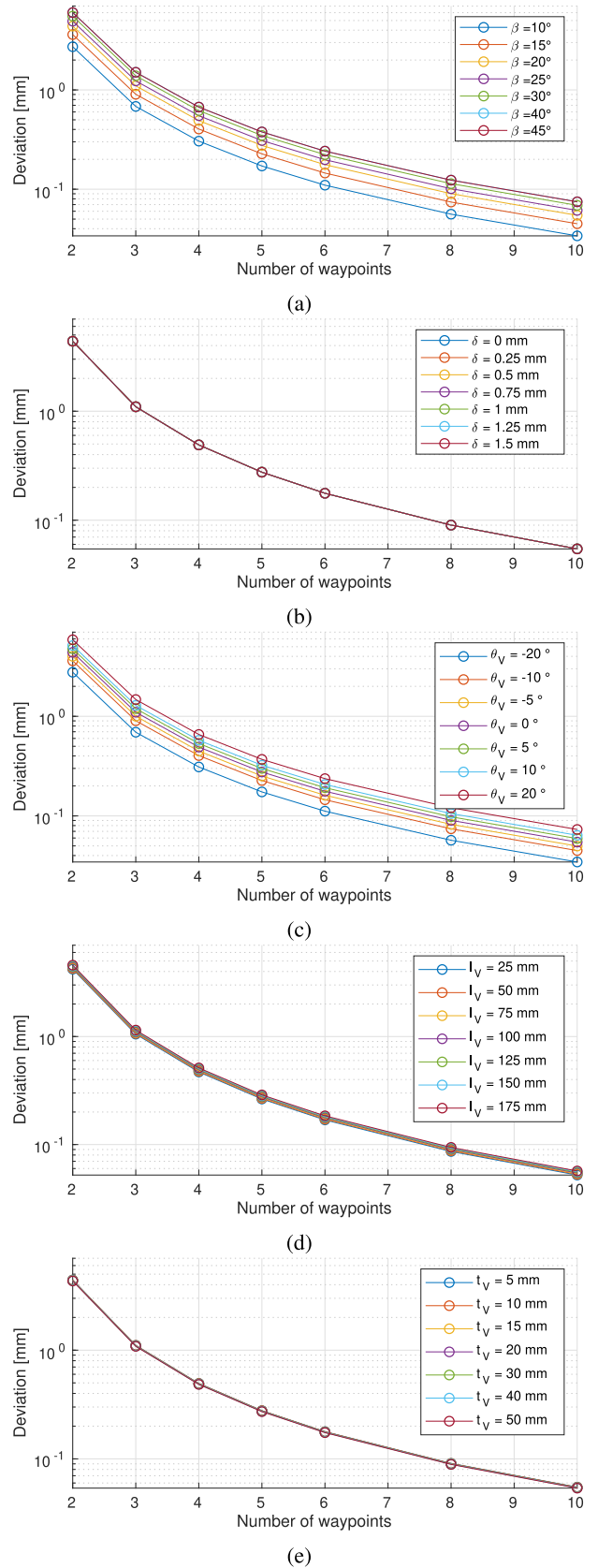
FIGURE 6. Influence of the number of waypoints per line in the maximum deviation from the straight light between waypoints. Please note that the vertical axes use a logarithmic scale.

FIGURE 7. Scheme of the projection of straight lines on a target placed at a nominal distance. In order to achieve this, the points at the outside surface of the viewport do not lie exactly on top of each other. Therefore, the laser surface is actually a cone with very slight curvatures. As a consequence, when the target lies at a different distance, the waypoints will not be exactly on top of each other. Please note that the curvature of this surface is in reality much lower than drawn.

the double refraction, which mainly depend on β [39] (see figure 4). This way, it can compute the required angles to project a given number of waypoints at their desired positions. Nonetheless, the movement of the mirror between waypoints still follows the distorted trajectories shown in figure 4, introducing a distortion with respect to the corresponding straight line.

The deviation Δ of the actual light pattern from the desired one largely depends on the number of waypoints used per line, as shown in figure 5. Intuitively, the deviation Δ should decrease when more waypoints per line are used: the smaller the distance between two consecutive waypoints, also the smaller the deviation Δ. The actual evolution is depicted in figure 6.

Some conclusions can be drawn from these plots. In general, the higher the number of waypoints per line, the lower the deviation. However, this introduces a trade-off, since increasing the number of waypoints per line may in principle mean higher memory requirements and scan time.

The deviation can also be minimized by reducing β (see figure 6a). This is an expected result, since a smaller β naturally introduces less deviation, as seen in figure 4. However, this reduction is usually limited in practice by the laser module (or an alternative mirror combination), which would obstruct the reflected light for $\beta \to 0°$. Another reason to keep β as small as possible is to increase the effective reflective area of the mirror (in reality, a laser ray has a certain beam diameter and is not a 1D line).
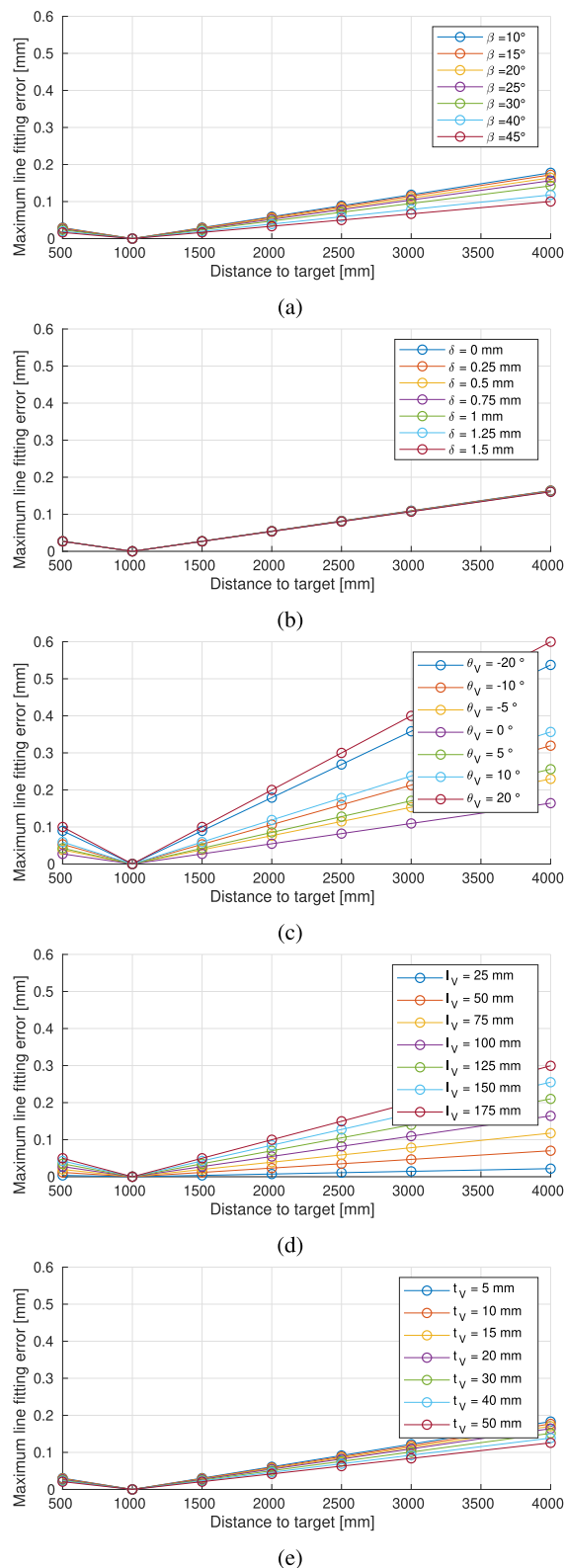
FIGURE 8. Maximum line fitting error when the actual scan plane does not necessarily lie at the nominal distance of 1000 mm.

In a similar fashion, increasing θ_V in the negative direction has a positive influence in the pattern deviation (see figure 6c). However, making $\theta_V \neq 0°$ has other implications

(see section IV-B2). The rest of the parameters (δ, l_V and t_V) have a much smaller influence (see figure 6b, 6d and 6e).

2) DIFFERENT TARGET DISTANCE

The set of angles required to project straight lines depends on the distance to the target, so a certain value needs to be chosen as nominal. However, during the actual scanning, the target may lie at a different distance, which is not known a priori. This fact results in the projection points corresponding to the same line not lying exactly one on top of the other. The reason for it is that the double refraction causes points $\boldsymbol{R}^i$ in figure 1 not to form a perfectly straight line. Therefore, the outgoing light planes are in reality curved surfaces with very slight curvatures (see figure 7).

In order to assess the actual magnitude of the error, a straight line was fitted using least squares to each line of waypoints $\boldsymbol{S}^i$. The metric used is the maximum distance from the points in the pattern to their corresponding fitted line. Results are shown in figure 8.

It can be seen that the most influential parameters are viewport distance and orientation. With a wise choice of a small viewport distance l_V and with $\theta_V = 0°$, the maximum distance to the corresponding fitted line is well below 0.05 mm (see figures 8c and 8d), even if the scanned target lies at a distance of 4 m (whereas the angles have been calibrated for 1 m). The rest of the parameters (β, δ and t_V) have a much lower influence on the magnitude of this error (see figures 8a, 8b and 8e).
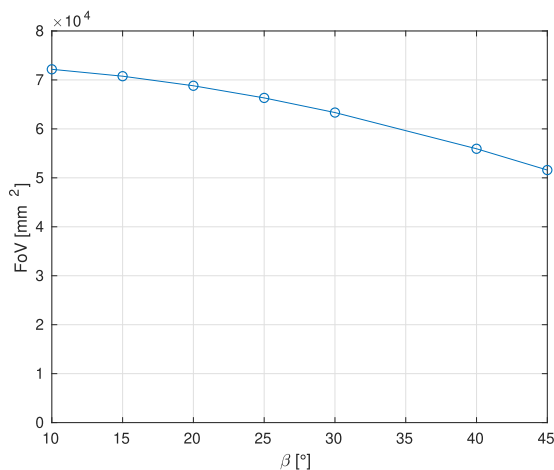

FIGURE 9. FoV at a distance of 1 m.

C. FIELD OF VIEW

A relevant performance characteristic of a scanner is its FoV, which should be as big as possible. In the presented model, the area covered by the FoV is mainly dependent on β, as plotted in figure 9. According to this graph, reducing β also contributes to increasing the scanner's FoV.

V. CONCLUSION AND FUTURE WORK

The model presented in this paper constitutes a tool to prove that using a biaxial mirror as deflecting element in an underwater 3D scanner can minimize the distortions introduced by a flat refractive viewport. Moreover, the model is also useful to study the theoretical performance of the scanner for a set of variable parameters. One of the first conclusions that can be drawn is that calibrating properly all the parameters is essential for an accurate light projection, as has been proved with synthetic data.

Furthermore, the model can be used to have a better understanding with respect to the optimal nominal values of the different parameters. It has been proved that the angle β should be kept small, so a reasonable value for the MEMS orientation with respect to the laser could be $\theta_M \approx -80°$. The flat viewport should be placed close to the MEMS (l_V as small as possible) and perpendicular to the reflected laser ray ($\theta_V \approx 0°$). Viewport thickness does not influence much, so in practice its value will mainly depend on mechanical and production requirements. It is also important to keep $\delta \approx 0°$, so laser and MEMS should be as well aligned as possible. With this configuration and using a high enough number of waypoints, the errors from the studied sources should not introduce noticeable deviations in the straightness of the laser lines, even when scanning at different distances.

Coming back to the contributions of this work introduced in section I, it has been proved that the presented approach can in principle reduce significantly the 3D reconstruction time while keeping a high accuracy. The authors in [11] claim that using a 1-DoF mirror, the maximum fitting error at a distance of 100 mm was 0.195 mm using elliptic cones and 4.05 mm using planes. In our approach with a 2-DoF mirror, and using the discussed nominal values for each parameter, the maximum fitting error using planes is less than 0.1 mm at a 4 m distance.

Finally, changes of the index of refraction of the water η_1 should be taken into account. By following these recommendations, submillimetric accuracy in the projection of straight lines could in principle be achieved for a wide range of distances to the target.

The next step in this line of research should be building a first prototype of the scanner using the knowledge presented in this paper. Once it has been built, its implementation and testing will likely yield hardware-related sources of error which have not been considered yet. Examples of these types of sources are limitations in the MEMS dynamic control and in the accuracy of the calibration result.

APPENDIX A
GEOMETRICAL CONCEPTS

This appendix first gathers three well-known principles, namely reflection, refraction and line-plane intersection, upon which the mathematical model is built. Then, coordinate composition to transform points and vectors into different reference frames are reviewed.

1) REFLECTION (figure 10a)

The direction vector of the light ray resulting from the reflection of a ray with vector $\boldsymbol{v}_{in}$ at a surface with normal $\boldsymbol{n}$

(a) Reflection.   (b) Refraction.
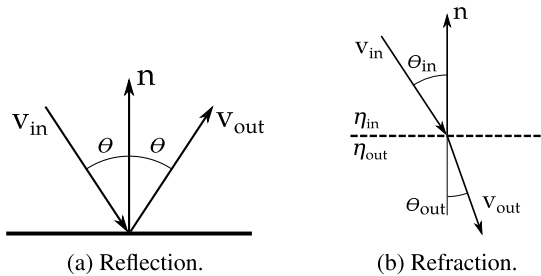
FIGURE 10. The direction of a light ray impacting on a surface changes due to either reflection or refraction, mainly depending on the properties of the surface material.

(given that v_{in} and n are unit vectors) is computed as:

$$v_{out} = v_{in} - 2\,(v_{in} \cdot n)\,n \tag{18}$$

2) REFRACTION (figure 10b)

In case a light ray with vector v_{in} encounters a refractive surface with normal n that separates two media with different refraction coefficients (η_{in} and η_{out}, respectively), and assuming that v_{in} and n are unit vectors, the direction vector of the resulting refracted ray can be expressed as:

$$v_{out} = \frac{\eta_{in}}{\eta_{out}}\,(n \times (-n \times v_{in}))$$

$$-n\sqrt{1 - \left(\frac{\eta_{in}}{\eta_{out}}\right)^2 (n \times v_{in}) \cdot (n \times v_{in})} \tag{19}$$

3) LINE-PLANE INTERSECTION

The intersection point P between a line $l = l_0 + \lambda v$ and a plane $\pi \equiv n \cdot x = d$ is computed as:

$$P = l \cap \pi = \frac{d - n \cdot l_0}{n \cdot v}\,v + l_0 \tag{20}$$

As seen here, a line is defined by a point and a direction vector $l = (l_0, v)$, whereas a plane is defined by its normal vector and the distance to the reference frame $\pi = (n, d)$.

4) 3D POSE COMPOSITION

The pose of a given coordinate frame A with respect to the world coordinate frame W is given by ${}^{\{W\}}\xi_{\{A\}}$ but, for the sake of readability, from now on it will be named as ξ_A. In 3D space, it is made up of 6 DoF:

$$\xi_A = [x\ y\ z\ \phi\ \theta\ \psi]^T \tag{21}$$

In order to change the reference frame in which the 3D coordinates of a point are expressed, the following equation is generally used:

$$^{\{W\}}P = {}^{\{W\}}t_{\{A\}} + {}^{\{W\}}R_{\{A\}}\,{}^{\{A\}}P, \tag{22}$$

where ${}^{\{W\}}t_{\{A\}}$ is the relative translation of $\{A\}$ with respect to $\{W\}$ and ${}^{\{W\}}R_{\{A\}}$ is the relative rotation of $\{A\}$ with respect to $\{W\}$. This operation is called composition and can be expressed in a more compact form:

$$^{\{W\}}P = \xi_A \oplus {}^{\{A\}}P \tag{23}$$

A more detailed explanation of compound geometrical relationships in 3D can be found in the appendix A of [45]. The coordinates of a vector can be expressed with respect to a different coordinate frame by simply rotating it:

$$^{\{W\}}v = {}^{\{W\}}R_{\{A\}}\,{}^{\{A\}}v, \tag{24}$$

Lines and planes can be characterized by using one point and one vector. A line is defined by any arbitrary point on it and its direction vector, whereas a plane is represented by any arbitrary point on it and its normal vector. Therefore, expressing a line or a plane with respect to a different reference frame boils down to applying the corresponding transformation to its defining point and vector.

ABBREVIATIONS

|	
AOD	acousto-optic deflector
AUV	autonomous underwater vehicle
DoF	degree of freedom
EOD	electro-optic deflector
FoV	field of view
LiDAR	light detection and ranging
LLS	laser line scanner
MEMS	microelectromechanical system
SfM	structure from motion
SONAR	sound navigation ranging
UUV	unmanned underwater vehicle

REFERENCES

[1] K. Himri, P. Ridao, N. Gracias, A. Palomer, N. Palomeras, and R. Pi, "Semantic SLAM for an AUV using object recognition from point clouds," *IFAC-PapersOnLine*, vol. 51, no. 29, pp. 360–365, 2018. [Online]. Available: https://linkinghub.elsevier.com/retrieve/pii/S2405896318321864

[2] A. Palomer, P. Ridao, and D. Ribas, "Inspection of an underwater structure using point-cloud SLAM with an AUV and a laser scanner," *J. Field Robot.*, vol. 36, no. 8, pp. 1333–1344, Dec. 2019.

[3] A. Palomer, P. Ridao, D. Youakim, D. Ribas, J. Forest, Y. Petillot, A. P. Monfort, and P. J. Sanz, "3D laser scanner for underwater manipulation," *Sensors*, vol. 18, no. 4, pp. 1–14, 2018.

[4] F. R. Dalgleish, S. Tetlow, and R. L. Allwood, "Experiments in laser-assisted visual sensing for AUV navigation," *Control Eng. Pract.*, vol. 12, no. 12, pp. 1561–1573, Dec. 2004. [Online]. Available: https://ac.els-cdn.com/S0967066103002594/1-s2.0-S0967066103002594-main.pdf?_tid=7d62f36a-e123-4310-a955-cff1e6446ed1&acdnat=1548408210_461d9c24e11c75c9fce5244ac192b6e6

[5] M. Massot-Campos and G. Oliver-Codina, "Optical sensors and methods for underwater 3D reconstruction," *Sensors*, vol. 15, no. 12, pp. 31525–31557, Dec. 2015. [Online]. Available: http://www.mdpi.com/1424-8220/15/12/29864

[6] S. T. Digumarti, G. Chaurasia, A. Taneja, R. Siegwart, A. Thomas, and P. Beardsley, "Underwater 3D capture using a low-cost commercial depth camera," in *Proc. IEEE Winter Conf. Appl. Comput. Vis. (WACV)*, Mar. 2016, pp. 1–9. [Online]. Available: http://ieeexplore.ieee.org/document/7477644/

[7] A. Anwer, S. S. Azhar Ali, A. Khan, and F. Meriaudeau, "Underwater 3-D scene reconstruction using kinect v2 based on physical models for refraction and time of flight correction," *IEEE Access*, vol. 5, pp. 15960–15970, 2017. [Online]. Available: http://ieeexplore.ieee.org/document/8000305/

[8] S. Chourasiya, P. K. Mohapatra, and S. Tripathi, "Non-intrusive underwater measurement of mobile bottom surface," *Adv. Water Resour.*, vol. 104, pp. 76–88, Jun. 2017. [Online]. Available: https://linkinghub.elsevier.com/retrieve/pii/S0309170817302385

[9] S. Chi, Z. Xie, and W. Chen, "A laser line auto-scanning system for underwater 3D reconstruction," *Sensors*, vol. 16, no. 9, p. 1534, Sep. 2016. [Online]. Available: http://www.mdpi.com/1424-8220/16/9/1534

[10] A. Palomer, P. Ridao, J. Forest, and D. Ribas, "Underwater laser scanner: Ray-based model and calibration," *IEEE/ASME Trans. Mechatronics*, vol. 24, no. 5, pp. 1986–1997, Oct. 2019.

[11] A. Palomer, P. Ridao, D. Ribas, and J. Forest, "Underwater 3D laser scanners: The deformation of the plane," in *Sensing and Control for Autonomous Vehicles* (Lecture Notes in Control and Information Sciences), vol. 474. Cham, Switzerland: Springer, 2017, pp. 73–88, doi: 10.1007/978-3-319-55372-6_4.

[12] F. Bruno, G. Bianco, M. Muzzupappa, S. Barone, and A. V. Razionale, "Experimentation of structured light and stereo vision for underwater 3D reconstruction," *ISPRS J. Photogramm. Remote Sens.*, vol. 66, no. 4, pp. 508–518, Jul. 2011. [Online]. Available: www.elsevier.com/locate/isprsjprs

[13] M. Castillón, A. Palomer, J. Forest, and P. Ridao, "State of the art of underwater active optical 3D scanners," *Sensors*, vol. 19, no. 23, p. 5161, Nov. 2019. [Online]. Available: https://www.mdpi.com/1424-8220/19/23/5161

[14] A. Sedlazeck and R. Koch, "Calibration of housing parameters for underwater stereo-camera rigs," in *Proc. Brit. Mach. Vis. Conf.*, 2011, pp. 1–11. [Online]. Available: http://www.mip.informatik.uni-kiel.de

[15] A. Jordt-Sedlazeck and R. Koch, "Refractive structure-from-motion on underwater images," in *Proc. IEEE Int. Conf. Comput. Vis.*, Dec. 2013, pp. 57–64.

[16] K. Istenič, N. Gracias, A. Arnaubec, J. Escartín, and R. Garcia, "Automatic scale estimation of structure from motion based 3D models using laser scalers in underwater scenarios," *ISPRS J. Photogramm. Remote Sens.*, vol. 159, pp. 13–25, Jan. 2020.

[17] P. Risholm, J. Thorstensen, J. T. Thielemann, K. Kaspersen, J. Tschudi, C. Yates, C. Softley, I. Abrosimov, J. Alexander, and K. H. Haugholt, "Real-time super-resolved 3D in turbid water using a fast range-gated CMOS camera," *Appl. Opt.*, vol. 57, no. 14, pp. 3927–3937, 2018. [Online]. Available: http://ao.osa.org/abstract.cfm?URI=ao-57-14-3927, doi: 10.1364/AO.57.003927.

[18] M. Massot-Campos and G. Oliver-Codina, "Underwater laser-based structured light system for one-shot 3D reconstruction," in *Proc. IEEE Sensors*, Nov. 2014, pp. 1138–1141. [Online]. Available: http://ieeexplore.ieee.org/lpdocs/epic03/wrapper.htm?arnumber=6985208

[19] M. Bleier and A. Nüchter, "LOW-cost 3D laser scanning in air orwater using self-calibrating structured light," *ISPRS Int. Arch. Photogramm., Remote Sens. Spatial Inf. Sci.*, vol. XLII-2/W3, pp. 105–112, Feb. 2017. [Online]. Available: https://www.int-arch-photogramm-remote-sens-spatial-inf-sci.net/XLII-2-W3/105/2017/isprs-archives-XLII-2-W3-105-2017.pdf

[20] P. Risholm, T. Kirkhus, and J. T. Thielemann, "High-resolution structured light d sensor for autonomous underwater inspection," in *Proc. OCEANS MTS/IEEE Charleston*, Oct. 2018, pp. 1–5. [Online]. Available: https://ieeexplore.ieee.org/document/8604930/

[21] F. Lopes, H. Silva, J. M. Almeida, A. Martins, and E. Silva, "Structured light system for underwater inspection operations," in *Proc. OCEANS Genova*, May 2015, pp. 1–6. [Online]. Available: http://ieeexplore.ieee.org/document/7271564/

[22] C. C. Constantinou, S. G. Loizou, and G. P. Georgiades, "An underwater laser vision system for relative 3-D posture estimation to mesh-like targets," in *Proc. IEEE/RSJ Int. Conf. Intell. Robots Syst. (IROS)*, Oct. 2016, pp. 2036–2041. [Online]. Available: http://ieeexplore.ieee.org/document/7759320/

[23] A. Bodenmann, B. Thornton, and T. Ura, "Generation of high-resolution three-dimensional reconstructions of the seafloor in color using a single camera and structured light," *J. Field Robot.*, vol. 34, no. 5, pp. 833–851, Aug. 2017, doi: 10.1002/rob.21682.

[24] G. Matos, P. D. Buschinelli, and T. Pinto, "Underwater laser triangulation sensor model with flat refractive interfaces," *IEEE J. Ocean. Eng.*, vol. 45, no. 3, pp. 937–945, Apr. Jul. 2020. [Online]. Available: https://ieeexplore.ieee.org/document/8644043/

[25] *2G Robotics. Uls-200*. Accessed: Apr. 4, 2020. [Online]. Available: https://www.2grobotics.com/products/underwater-laser-scanner-uls-200/

[26] M. Imaki, H. Ochimizu, H. Tsuji, S. Kameyama, T. Saito, S. Ishibashi, and H. Yoshida, "Underwater three-dimensional imaging laser sensor with 120-deg wide-scanning angle using the combination of a dome lens and coaxial optics," *Opt. Eng.*, vol. 56, no. 3, Oct. 2016, Art. no. 031212. [Online]. Available: http://opticalengineering.spiedigitallibrary.org/article.aspx?doi=10.1117/1.OE.56.3.031212

[27] Luminar Technologies, Inc. *Lidar*. Accessed: Mar. 28, 2020. [Online]. Available: https://www.luminartech.com/

[28] Velodyne Lidar, Inc. *Lidar*. Accessed: Mar. 28, 2020. [Online]. Available: https://velodynelidar.com/

[29] Quanergy Systems, Inc. *Lidar*. Accessed: Mar. 28, 2020. [Online]. Available: https://quanergy.com/technology-2/#LiDAR

[30] Ouster, Inc. *Lidar*. Accessed: Mar. 28, 2020. [Online]. Available: https://ouster.com/

[31] Valeo. *Valeo Scala*. Accessed: Mar. 28, 2020. [Online]. Available: https://www.valeo.com/en/valeo-scala/

[32] Ledartech. *Lidar*. Accessed: Mar. 28, 2020. [Online]. Available: https://leddartech.com/

[33] Blickfeld GmbH. *MEMS-Based Lidar*. Accessed: Mar. 28, 2020. [Online]. Available: https://www.blickfeld.com/technology/

[34] Mirrorcle Technologies, Inc. *MEMS Mirrors Catalogue*. Accessed: Mar. 28, 2020. [Online]. Available: https://www.mirrorcletech.com/wp/products/mems-mirrors/

[35] K. K. H. Photonics. *MEMS Mirrors Catalogue*. Accessed: Mar. 28, 2020. [Online]. Available: https://www.hamamatsu.com/jp/en/product/optical-components/mems-mirror/index.html

[36] S. T. S. Holmstrom, U. Baran, and H. Urey, "MEMS laser scanners: A review," *J. Microelectromech. Syst.*, vol. 23, no. 2, pp. 259–275, Apr. 2014. [Online]. Available: http://ieeexplore.ieee.org/document/6714402/

[37] M. Brown and H. Urey, "MEMS Microdisplays," in *Handbook of Visual Display Technology*. Berlin, Germany: Springer, 2015, pp. 1–15. [Online]. Available: http://link.springer.com/10.1007/978-3-642-35947-7_128-2

[38] Y. Song, R. M. Panas, and J. B. Hopkins, "A review of micromirror arrays," *Precis. Eng.*, vol. 51, pp. 729–761, Jan. 2018. [Online]. Available: https://www.sciencedirect.com/science/article/pii/S0141635917302210

[39] M. Hafez, T. Sidler, and R.-P. Salathé, "Study of the beam path distortion profiles generated by a two-axis tilt single-mirror laser scanner," *Opt. Eng.*, vol. 42, no. 4, pp. 1048–1057, Apr. 2003. [Online]. Available: http://opticalengineering.spiedigitallibrary.org/article.aspx?doi=10.1117/1.1557694

[40] P. Bechtold, R. Hohenstein, and M. Schmidt, "Evaluation of disparate laser beam deflection technologies by means of number and rate of resolvable spots," *Opt. Lett.*, vol. 38, no. 16, p. 2934, Aug. 2013. [Online]. Available: https://www.osapublishing.org/abstract.cfm?URI=ol-38-16-2934

[41] G. R. B. E. Römer and P. Bechtold, "Electro-optic and acousto-optic laser beam scanners," *Phys. Procedia*, vol. 56, pp. 29–39, Jan. 2014. [Online]. Available: www.sciencedirect.com

[42] S. Agarwal and K. Mierle. *Ceres Solver*. Accessed: Mar. 28, 2020. [Online]. Available: http://ceres-solver.org

[43] E. Hecht, *Optics*, 5th ed. London, U.K.: Pearson, 2017. [Online]. Available: www.pearsonglobaleditions.com

[44] R. W. Austin and G. Halikas, "The index of refraction of seawater," Visibility Lab., Univ. California, Oakland, CA, USA, Tech. Rep. 76-1, 1976. [Online]. Available: http://misclab.umeoce.maine.edu/education/VisibilityLab/reports/SIO_76-1.pdf

[45] R. Smith, M. Self, and P. Cheeseman, "Estimating uncertain spatial relationships in robotics," in *Autonomous Robot Vehicles*. New York, NY, USA: Springer, 1990, pp. 167–193. [Online]. Available: https://link.springer.com/chapter/10.1007/978-1-4613-8997-2_14

MIGUEL CASTILLÓN received the B.Sc. degree in industrial engineering from the University of Zaragoza, Spain, in 2015, and the M.Sc. degree in mechanical engineering from KU Leuven, Belgium, in 2018. He is currently pursuing the Ph.D. degree in robotics with the University of Girona, Spain. His research interests include computer vision applied to robotics and autonomous navigation.
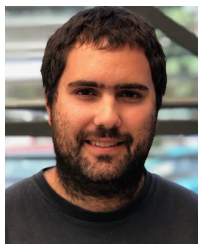
ALBERT PALOMER received the M.Sc. degree in industrial engineering, the M.Sc. degree in information technologies and automation, and the Ph.D. degree from the University of Girona, in 2012, 2013, and 2018, respectively. In 2012, he joined the Underwater Robotics Research Center (CIRS), University of Girona. He is currently a Software Engineer with IQUA Robotics. His research interests include AUVs, on underwater 3D perception, and underwater navigation.

JOSEP FOREST received the B.Sc. degree in industrial informatics from the University of Girona, in 1992, the M.Sc. degree in electronics engineering from the Autonomous University of Barcelona, in 1998, and the Ph.D. degree from the University of Girona, in 2004. His research interests include 3D-machine vision, including laser triangulation, calibration, detection, Point Cloud processing, usability of 3D applied to the industry for dimensional testing, and quality control applications.

PERE RIDAO (Member, IEEE) received the Ph.D. degree in industrial engineering from the University of Girona, Spain, in 2001. He is currently the Director of the Computer Vision and Robotics Research Institute (VICOROB), the Head of the Underwater Robotics Research Center (CIRS), and an Associate Professor with the Department of Computer Engineering, University of Girona. Since 1997, he has been participated in 24 research projects (15 European and nine National), he is an author of more than 100 publications, and he has directed nine Ph.D. thesis (four more under direction) and 14 M.S. thesis. He is also a coauthor of four licenses and one Spanish/European patent, being the Co-Founder of Iqua Robotics S.L. spin-off company. His research interests include designing and developing Autonomous Underwater Vehicles for 3D Mapping and Intervention. He has served as the Chair of the IFAC's Technical Committee on Marine Systems.

• • •